How Do Regional Distributions of Daily Precipitation Change under Warming?

ROBIN CHADWICK,[a,b] ANGELINE G. PENDERGRASS,[c,d] LINCOLN MUNIZ ALVES,[e] AND AUREL MOISE[f]

[a] *Met Office Hadley Centre, Exeter, United Kingdom*
[b] *Global Systems Institute, Department of Mathematics, University of Exeter, Exeter, United Kingdom*
[c] *National Center for Atmospheric Research, Boulder, Colorado*
[d] *Cornell University, Ithaca, New York*
[e] *National Institute for Space Research (INPE), São José dos Campos, São Paulo, Brazil*
[f] *Centre for Climate Research, Singapore*

(Manuscript received 11 November 2020, in final form 15 December 2021)

ABSTRACT: Global warming is changing the intensity distribution of daily precipitation, with an increased frequency of heavy precipitation and reduced frequency of light/moderate precipitation in general circulation model (GCM) projections. Projected future CMIP5 GCM changes in regional daily precipitation distribution can be described by a combination of two idealized modes: a frequency decrease mode, representing a reduction in the frequency of precipitation at all rain rates; and a frequency shift mode, where the distribution shifts toward heavier rain rates. A decrease in daily precipitation frequency and an increase in intensity are projected in most regions, but the magnitude of change shows large regional variations. The two modes generally capture the projected shift from light/moderate to heavy rain rates but do not recreate GCM changes at the very highest and lowest rain rates. We propose a simple framework for deep convective precipitation change based on the dry static energy (DSE) budget, which provides a physical explanation of these idealized modes in regions and seasons where deep convection dominates precipitation. One possibility is that a frequency decrease mode is driven by increased convective inhibition (CIN). In this DSE framework, increased moisture under warming could influence the shape of the precipitation intensity distribution, particularly at the highest rain rates, but does not govern the overall magnitude of the shift to heavier rain rates, which is not well described by the Clausius–Clapeyron relationship. Changes in daily regional precipitation are not free to respond only to local changes (in e.g., moisture) but are also constrained by the DSE budget, particularly by DSE transport associated with the large-scale circulation.

KEYWORDS: Climate change; Climate models; Precipitation; Convection; Energy transport

1. Introduction

Global warming is altering the intensity distribution of daily precipitation, with an increase in the observed frequency of heavy rainfall (Allan et al. 2010; Donat et al. 2013; Alexander et al. 2006; Min et al. 2011; Fischer and Knutti 2016; Zhang and Zhou 2019). Climate projections suggest that this trend will continue into the future (e.g., Fischer et al. 2014; O'Gorman 2015), including an increase in the intensity of precipitation extremes (e.g., Collins et al. 2013; Emori and Brown 2005; O'Gorman 2015; Pfahl et al. 2017; Bador et al. 2018; Fowler et al. 2021), and will be accompanied by a decreased frequency of light-to-moderate precipitation events (Sun et al. 2007). Globally, a small overall decrease in the frequency of precipitation (Pendergrass and Hartmann 2014a) is projected, but regionally there are large changes in the number of dry days, which increase significantly over some land regions (Polade et al. 2014). The combination of these precipitation changes could lead to greater risk of flooding, but also longer dry periods. Importantly, precipitation change under warming and its associated impacts are not homogeneous across the globe but have substantial regional variations (Collins et al. 2013; Chadwick et al. 2013; Pfahl et al. 2017), which have been explored less comprehensively than global-mean changes despite their potentially large societal impacts.

Pendergrass and Hartmann (2014b) described the change in the globally aggregated distribution of daily precipitation accumulations (referred to hereafter, for brevity, as rain rates) in terms of two idealized modes: an increase mode whereby the total amount of precipitation at all rain rates increases, and a shift mode whereby the intensity of rainfall increases and the amount distribution "shifts" from lighter to heavier rain rates. A combination of these modes was shown to provide a good description of the global change in daily precipitation distribution projected by the CMIP5 ensemble mean. However, at the regional scales relevant to climate change impacts, dynamical changes strongly influence changes in precipitation distributions (Pfahl et al. 2017; Oueslati et al. 2019) and the ability of the two idealized modes to represent changes in the distribution of daily precipitation at these scales has not previously been assessed. If the two-mode model does work at regional scales, this would provide a convenient way of quantifying regional variations in changes of the precipitation intensity distribution. Here, we will make this assessment.

To consider whether the two-mode model of precipitation change that emerges from GCM projections is physically plausible, it is first necessary to explain the modes in terms of particular physical processes or constraints. One such physical constraint is the increase in atmospheric water vapor with warming under the Clausius–Clapeyron relationship at around 7% K^{-1} (Held and Soden 2006; Allan et al. 2014).

Corresponding author: Robin Chadwick, robin.chadwick@metoffice.gov.uk

DOI: 10.1175/JCLI-D-20-0864.1

This has often been linked to projected increases in the intensity and frequency of extreme rainfall (e.g., Allen and Ingram 2002; Pall et al. 2007; Kendon et al. 2019) and might also partly explain the more general shift of the daily precipitation distribution to heavier rain rates under warming. An increase in moisture would, however, not directly explain a decrease in the frequency of precipitation. A related hypothesis for precipitation changes over land that would explain a reduction in frequency (Dai et al. 2017) is that each storm removes 7% K^{-1} more moisture from the air but the change in surface evaporation and moisture convergence is smaller, leading to a greater time for moisture to be replenished, decreased near-surface relative humidity (RH), and a reduced overall frequency of storms. However, by itself a moisture increase mechanism would predict an increased intensity of all events in the daily precipitation distribution of around 7% K^{-1}, whereas the estimated magnitude of precipitation intensity increase (the shift mode) in the CMIP5 ensemble mean distribution is only 3.3% K^{-1} (Pendergrass and Hartmann 2014a). Therefore, increased moisture by itself does not seem to provide an explanation for the change in the daily precipitation intensity distribution projected by GCMs.

It has been suggested that precipitation cannot in general increase at 7% K^{-1} because on a global scale it is energetically constrained to balance global atmospheric radiative cooling (e.g., Allen and Ingram 2002; Stephens and Ellis 2008). A global mean increase in net atmospheric radiative cooling (or equivalently of net surface heating) of only 1%–3% K^{-1} in GCMs suggests that if precipitation intensity did increase by 7% K^{-1} then the overall global frequency of precipitation would have to substantially decline (Trenberth 1999). However, it is very unclear how this global constraint might filter down to the spatial scales at which precipitation occurs. In the present study, we will use the dry static energy (DSE) budget to examine how regional changes in daily precipitation distributions might be constrained by changes in radiative cooling and energy transport by the large-scale atmospheric circulation.

For precipitation associated with deep convection, another explanation of the changing frequency and intensity of events has been proposed (Rasmussen et al. 2017). It was suggested that increased convective inhibition (CIN) under warming leads to a greater barrier to the initiation of moderate intensity deep convective events, reducing the overall frequency of deep convection and precipitation. This could allow more time between each event for instability to build up, leading to increased convective available potential energy (CAPE) and more intense precipitation when deep convection does occur. Increased CIN under warming in convective regions has been found by several modeling studies (Pascale et al. 2017; Chen et al. 2020; Grabowski and Prein 2019; Kendon et al. 2019). In Chen et al. (2020) and Grabowski and Prein (2019) the increased CIN was mainly associated with a reduction in RH over land, which is driven by a greater increase of land temperatures than of the moisture supply from the oceans (Chadwick et al. 2016; Byrne and O'Gorman 2016), combined with changes in plant physiology and soil moisture (Berg et al. 2016). We will examine this CIN-based hypothesis and link it mathematically to the two idealized modes of Pendergrass and Hartmann (2014b).

In this study we will focus on the response of precipitation to a high greenhouse gas forcing scenario, in order to maximize the signal-to-noise of daily precipitation change on regional scales. We do not attempt to separate the influence of warming from the direct radiative or physical influences of GHG and aerosol forcing on daily precipitation, but previous work has found that these direct effects are also important (e.g., Douville and John 2021; Abbott and Cronin 2021). We use data from the CMIP5 ensemble, but changes in the intensity distribution of daily precipitation in CMIP6 appear to be similar to CMIP5 (Douville et al. 2021), so we expect our results and conclusions to also be relevant to CMIP6.

The study has two main parts. In the first, we adapt the two modes of Pendergrass and Hartmann (2014b) and apply them regionally to the CMIP5 ensemble to assess whether changes in the distribution of daily precipitation can be described by two idealized modes at regional scales. In the second part we focus on deep convective precipitation and propose a simple conceptual model using the DSE budget to provide a physical basis for the two-mode model at regional scales.

2. Data

We use daily precipitation data from 27 climate models from phase 5 of the Coupled Model Intercomparison Project (CMIP5; Taylor et al. 2012), from the coupled historical (years 1971–2000) and representative concentration pathway 8.5 (RCP8.5; years 2071–2100) experiments. RCP8.5 is a high-emissions scenario, which we use here in order to maximize the climate change signal in the precipitation response. These models are listed in Table 1 and only the first ensemble member of each model is used. The daily precipitation distributions shown here include data from all days within each experiment and time period. Note that in this study we use the term "intensity distribution" to refer to the distribution of daily mean precipitation intensities (i.e., daily precipitation accumulations).

3. Analysis of intensity distribution change

In this section we will adapt the two idealized modes of Pendergrass and Hartmann (2014b) and estimate them at regional scales for the CMIP5 ensemble, in order to assess whether the change in the daily intensity distribution of precipitation (i.e., the distribution of daily precipitation accumulations) can be described by these modes at regional scales. We begin by examining CMIP5 ensemble-mean summary statistics of regional daily precipitation changes.

The mean pattern of precipitation change (Fig. 1a) is dominated by dynamical changes in the large-scale circulation (Seager et al. 2010; Chadwick et al. 2013; Shepherd 2014; He and Soden 2015), with precipitation increases at higher latitudes, decreases over many subtropical ocean regions, and a mixed pattern of change over tropical and subtropical land. There is considerable intermodel uncertainty in these changes, with even the sign of change uncertain in many regions (Fig. 1a). The pattern of daily standard deviation change is similar (Fig. 1b) but generally slightly more positive (Fig. 1d), and has increases

TABLE 1. CMIP5 GCMs used in this study, together with the horizontal resolution of their atmospheric components (note that values may only be accurate near the equator depending on the grid used). Expansions of acronyms are available online at http://www.ametsoc.org/PubsAcronymList.

Modeling center	Model	Lat resolution (°)	Lon resolution (°)	Reference
CSIRO-BOM	ACCESS1.0	1.25	1.875	Bi et al. (2013)
CSIRO-BOM	ACCESS1.3	1.25	1.875	Bi et al. (2013)
GCESS	BNU-ESM	2.791	2.813	Ji et al. (2014)
CCCma	CanESM2	2.791	2.813	Chylek et al. (2011)
NCAR	CCSM4	0.942	1.25	Neale et al. (2010)
NSF-DOE-NCAR	CESM1-BGC	0.942	1.25	Neale et al. (2010)
CMCC	CMCC-CM	0.748	0.75	Scoccimarro et al. (2011)
CMCC	CMCC-CMS	3.711	3.75	Scoccimarro et al. (2011)
CNRM-CERFACS	CNRM-CM5	1.401	1.406	Voldoire et al. (2013)
CSIRO-QCCCE	CSIRO-Mk3.6.0	1.865	1.875	Jeffrey et al. (2013)
ICHEC	EC-Earth	1.122	1.122	Hazeleger et al. (2010)
LASG-CESS	FGOALS-g2	2.791	2.813	Li et al. (2013)
NOAA GFDL	GFDL CM3	2	2.5	Donner et al. (2011)
NOAA GFDL	GFDL-ESM2G	2.023	2	Dunne et al. (2012)
NOAA GFDL	GFDL-ESM2M	2.023	2.5	Dunne et al. (2012)
MOHC	HadGEM2-AO	1.25	1.875	Martin et al. (2011)
INM	INM-CM4	1.5	2	Volodin et al. (2010)
IPSL	IPSL-CM5A-LR	1.895	3.75	Dufresne et al. (2013)
IPSL	IPSL-CM5A-MR	1.268	2.5	Dufresne et al. (2013)
IPSL	IPSL-CM5B-LR	1.895	3.75	Hourdin et al. (2006)
MIROC	MIROC5	1.401	1.406	Watanabe et al. (2010)
MIROC	MIROC-ESM	2.791	2.813	Watanabe et al. (2011)
MIROC	MIROC-ESM-CHEM	2.791	2.813	Watanabe et al. (2011)
MPI-M	MPI-ESM-LR	1.865	1.875	Stevens et al. (2013)
MPI-M	MPI-ESM-MR	1.865	1.875	Stevens et al. (2013)
MRI	MRI-CGCM3	1.121	1.125	Yukimoto et al. (2012)
NCC	NorESM1-M	1.895	2.5	Bentsen et al. (2013)

over almost all land regions (see also Pendergrass et al. 2017; Brown et al. 2017). Therefore, the change in standard deviation is not solely related to the change in the mean, as in that case both statistics would scale together (i.e., the coefficient of variation would be constant), so an additional change in the width and/or shape of the distribution is implied. A change in the shape of the distribution is also implied by changes in skewness (Fig. 1d), which are generally positive, but are opposite in sign to the mean and standard deviation change over many ocean regions.

a. *Two modes of precipitation change*

Pendergrass and Hartmann (2014b) introduced two idealized modes that can be combined to describe the change in the globally aggregated daily rainfall intensity distribution under warming. Daily precipitation totals (rain rates) are first divided into logarithmic bins. Logarithmic bins are used in order to make the amount of data in each bin more even, and also because log-space provides some useful mathematical properties for the derivation of the two modes.

To produce a histogram of the rain-rate distribution in "amount space", the rain rate is multiplied by the normalized frequency of precipitation at each rain rate. Two idealized modes of transformation are applied to this distribution to simulate changes under warming: an amount increase mode (Fig. 2a) and an amount shift mode (Fig. 2b).

The increase mode is illustrated schematically in Fig. 2a and corresponds to a fractionally constant increase I in the rain amount at each rain rate:

$$A'(\ln P) = (1 + I)A(\ln P), \tag{1}$$

where $A(\ln P)$ is the control precipitation amount corresponding to rain rate P and $A'(\ln P)$ is the perturbed precipitation amount under warming.

The shift mode is shown in Fig. 2b and corresponds to a shift of the precipitation amount distribution to higher rain rates by a constant fractional amount S. In log-space this is given by

$$A'(\ln P) = A(\ln P - S). \tag{2}$$

The amount modes fitted to the change in the ensemble mean of the globally aggregated daily precipitation distributions of the CMIP5 models are shown in Fig. 3a; see Pendergrass and Hartmann (2014b) for the derivation of the two modes and details of how the parameters are estimated. As found by Pendergrass and Hartmann (2014a) the combined modes capture the GCM changes at light/moderate and heavy rain rates very closely, but show smaller increases at the heaviest rain rates and larger decreases at very low rain rates than GCMs. Note that all GCMs have biases in their present-day precipitation distributions (e.g., Mehran et al. 2014) that

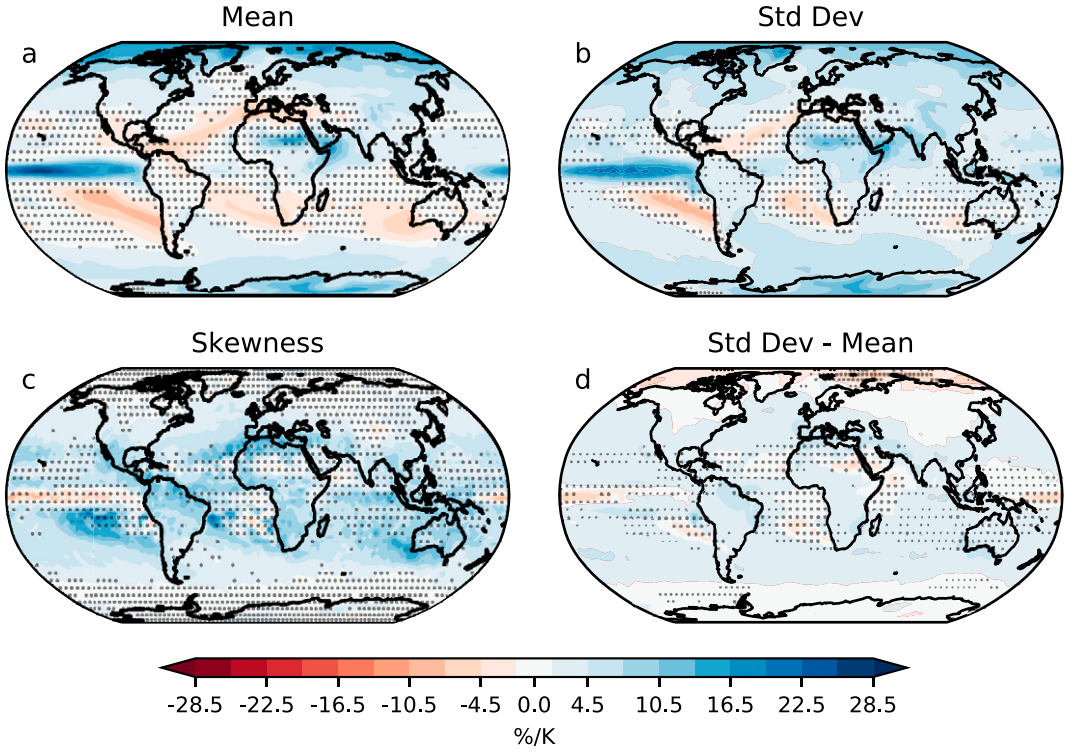

FIG. 1. CMIP5 ensemble mean changes (% K^{-1}) in daily precipitation accumulation between historical (1971–2000) and RCP8.5 (2071–100) experiments, showing the (a) mean, (b) standard deviation, and (c) skewness, and (d) the difference of (b) − (a). Stippling indicates regions where fewer than 80% of CMIP5 models agree on the sign of change.

may affect future projections, so this disagreement does not necessarily indicate that the two-mode model is incorrect at the lowest and highest rain rates.

Following Pendergrass and Hartmann (2014b), we quantify the error in the two-mode fit compared to the actual change in the GCM distribution, calculated as

$$\text{Error} = 100.0 \times \frac{\sum_i \left|\Delta P_{\text{shift},i} + \Delta P_{\text{inc},i} - \Delta P_{\text{GCM},i}\right|}{\sum_i \left|\Delta P_{\text{GCM},i}\right|}, \quad (3)$$

where $\Delta P_{\text{GCM},i}$ is the GCM precipitation change in rain-rate bin i, $\Delta P_{\text{shift},i}$ and $\Delta P_{\text{inc},i}$ are the precipitation change in bin i from the amount shift and amount increase modes respectively, vertical lines indicate absolute values, and the summations are over all nonzero rain-rate bins. For the CMIP5 ensemble mean globally aggregated distribution change (Fig. 3a) the error on the two-mode fit is 36%.

It can sometimes be more physically intuitive to work in precipitation frequency space, rather than amount space. It is possible to formulate two mathematically equivalent (degenerate) modes in precipitation frequency space, which provide an alternative perspective to the amount space modes. In this case we obtain a frequency shift mode and a frequency decrease mode (as opposed to the amount increase mode), as shown in Figs. 2c and 2d.

The frequency shift mode (Fig. 2d) has the same magnitude (S) as the amount shift mode (see the appendix for the derivation) and is given by

$$f'(\ln P) = f(\ln P - S), \quad (4)$$

where $f(\ln P)$ is the normalized frequency of events at rain rate P in the control climate and $f'(\ln P)$ is the perturbed frequency under warming.

The frequency decrease mode (Fig. 2c) is given by

$$f'(\ln P) = (1 + D) f(\ln P), \quad (5)$$

where D is a fractionally constant decrease in the frequency of occurrence at each rain rate (we assign the convention that negative values of D correspond to a decrease).

The amount increase and frequency decrease parameters are related to each other by the following equation (see the appendix for the derivation):

$$D = I - S. \quad (6)$$

Frequency modes were calculated for the CMIP5 ensemble mean from the amount modes using Eq. (6), and are shown in Fig. 3b. The increased frequency seen in GCMs at high rain rates is captured, and the decreased frequency at light/moderate rain rates is represented but is larger than in GCMs. However, working in frequency space highlights that the two idealized

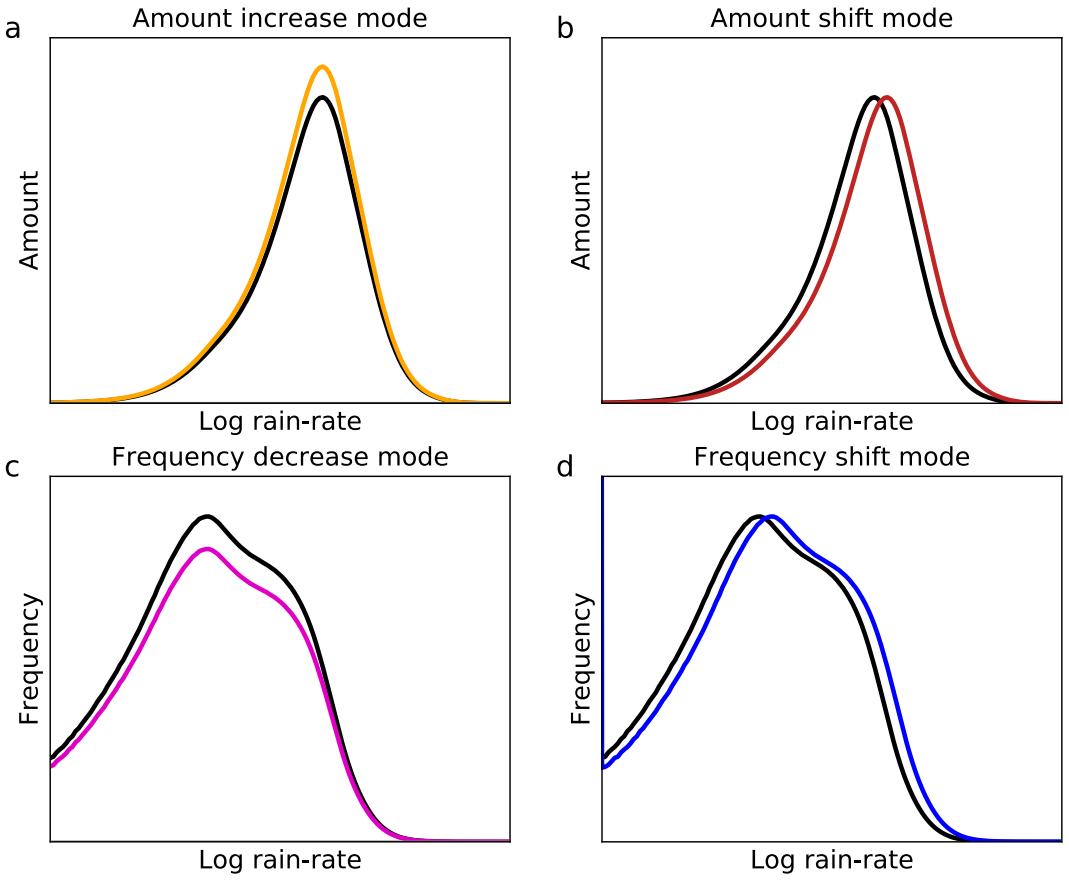

FIG. 2. Schematic of idealized modes describing changes in the globally aggregated daily precipitation intensity distribution. Black lines show the present-day distributions and colored lines show the idealized future distributions under warming. Plots shown (a) amount increase mode, (b) amount shift mode, (c) frequency decrease mode, and (d) frequency shift mode.

modes produce much larger decreases in precipitation at very low rain rates than GCMs. This is not obvious when working in precipitation amount space, as these lowest rain rates contribute very little to total precipitation. We calculated the frequency modes by converting from the amount modes using Eq. (6) rather than directly fitting the frequency modes in frequency space, because the disagreement between the two-mode model and GCMs at very low rain rates introduces large errors to the fit in frequency space but not in amount space.

Overall, the two idealized modes (either in amount or frequency space) capture the globally aggregated shift from light/moderate to heavy rain rates seen in GCMs, but do not agree with GCM changes at the very highest and lowest ends of the rain-rate spectrum. We will discuss the physical interpretation of the two-mode model in section 4. We next apply these modes at regional scales and assess their skill.

b. *Application to regional scales*

Climate models exhibit variable skill in the present-day representation of regional hydroclimate (Christenson et al. 2013; Wang et al. 2020) and this also affects confidence in future projections. Our aim here is not to validate regional precipitation projections, but only to assess whether the two-mode model is a useful description of GCM changes in regional daily precipitation distributions. To improve signal-to-noise when fitting the two-mode model to gridpoint precipitation distributions, and to highlight changes that are common across different GCMs, we focus on the CMIP5 ensemble mean. However, as was shown by Pendergrass and Hartmann (2014a) for the globally aggregated daily precipitation distribution, there is significant variation across individual climate models as to how closely their simulated regional changes are captured by the two-mode model.

The modes were now fitted separately at each grid point to the ensemble mean of the daily precipitation distributions of the CMIP5 models [again, using the fitting method of Pendergrass and Hartmann (2014b)]. The estimated parameters in amount and frequency space, and the error associated with the fit in amount space, are shown in Fig. 4. Note that although the amount increase mode (I) is positive and the frequency decrease mode (D) is negative in the globally aggregated distribution, this is not always true at regional scales, and both increases and decreases (positive and negative values of I and D) occur in both amount and frequency space. The shift mode parameter (S) has the same magnitude in both amount and frequency space, and

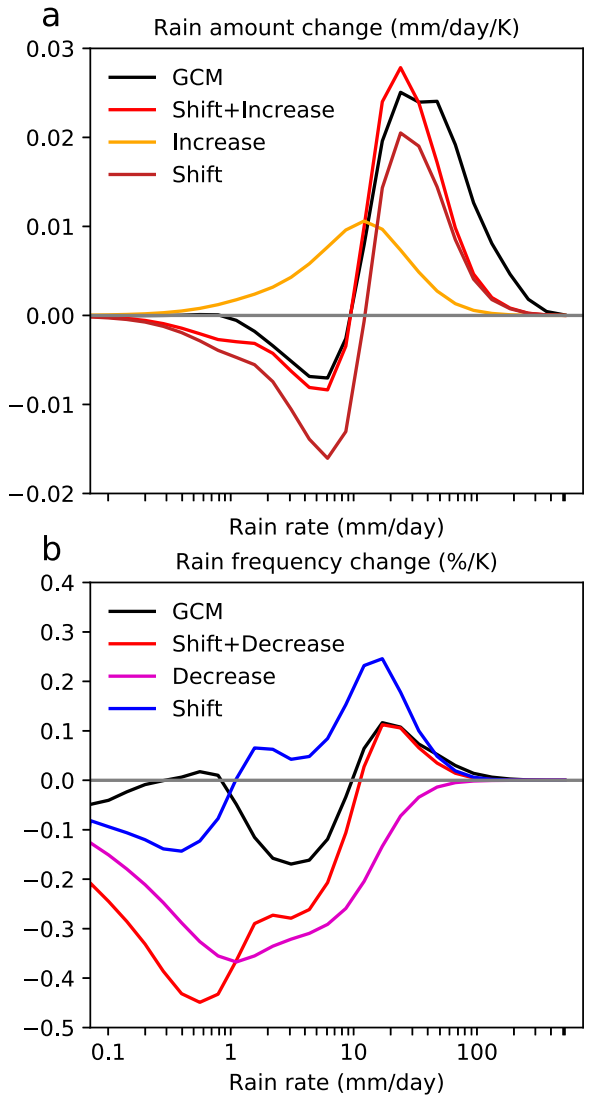

FIG. 3. CMIP5 ensemble mean changes (RCP8.5 − Historical) in the daily precipitation intensity distribution in (a) amount space and (b) frequency space. Black lines show GCM changes, red lines show the combination of shift and increase/decrease modes fitted to the GCM changes, and yellow/brown/blue/purple lines show the individual contributions of shift and increase/decrease modes to the fit.

can also have both positive and negative values on regional scales.

All parameters show distinct regional variations, and so are clearly not strongly constrained by the global mean distribution change. The amount increase mode (Fig. 4b) closely follows the mean pattern of precipitation change (Fig. 1a), with increases in some regions and decreases in others. Intermodel uncertainty on the sign of this mode (shown by stippling in Fig. 4b) is similar to the pattern of intermodel uncertainty in the sign of mean change (Fig. 1a). The frequency decrease mode (Fig. 4c) is more spatially consistent in sign, with decreased frequency over all but a few ocean regions, which tend to be those with a large mean increase in precipitation such as the equatorial Pacific. There is greater intermodel agreement on the sign of this change (see unstippled regions) over land and in the extratropical oceans than there is over the tropical and subtropical oceans. The shift mode (Fig. 4a) is also fairly spatially consistent in sign, with a shift to increased rain rates in all but a few subtropical ocean regions. Intermodel uncertainty on the sign of this mode is more likely to be high in regions where negative shifts are present in the ensemble mean. The pattern of uncertainty in the shift mode (stippling in Fig. 4a) also has some similarities with the pattern of uncertainty in the mean precipitation change (Fig. 1a).

Strong spatial variation in the magnitude of the shift mode suggests that the magnitude of shifts to heavier rain rates in regional intensity distributions is not primarily governed by boundary layer moisture increases via the Clausius–Clapeyron relationship (thermodynamic changes), as moisture increases show relatively little spatial variability (e.g., Chadwick et al. 2016). Instead, it appears to be more likely to be associated with the more spatially varying changes in large-scale circulation (dynamical changes), as has also been found for regional changes in precipitation extremes (Pfahl et al. 2017).

The relative error (Fig. 4d) on the estimation of the amount modes also varies by region, and is largest in those regions with negligible changes in mean precipitation, possibly because the signal-to-noise ratio of the response of the precipitation distribution to warming is likely to be smaller in these regions. Error values are larger for fits to individual model distributions (not shown), partly due to greater noise in the grid point daily precipitation distributions for individual models than for the ensemble mean. Note that this measure of error [Eq. (3)] is quite strict, and the two-mode model can in some cases capture the qualitative behavior of the GCM distribution change even when this error value is relatively high.

To further assess how the idealized modes perform on a regional basis, we selected a variety of small regions (shown as black boxes in Fig. 4) for which to plot the GCM precipitation distributions and the fitted modes. Regions were selected so that parameter and error values were coherent throughout each box (see Fig. 4) and also to sample a wide range of geographical regions, mean precipitation changes, parameters, and error values. Precipitation distributions were calculated at each grid point, averaged over the small regions, then fitted with the modes. These are shown in Figs. 5 and 6. We note that the process of fitting the two-mode model includes an assumption that changes in the precipitation distribution are relatively small (see Pendergrass and Hartmann 2014b), which may not be valid for the largest regional precipitation changes, so this is one reason for examining the regional fits in more detail.

Precipitation frequency and amount in the central equatorial Pacific (Figs. 5a,e) increases at all except the lowest rain rates. The modes capture this GCM behavior, despite overestimating the frequency change at low rain rates. In the off-equatorial Pacific region (Figs. 5b,f) there is a mean decrease in precipitation. This is reflected in a decrease in the amount and frequency at light/moderate rain rates, but there is still a small increase in precipitation amount at the lowest and highest rain rates. The two modes capture the GCM decrease at

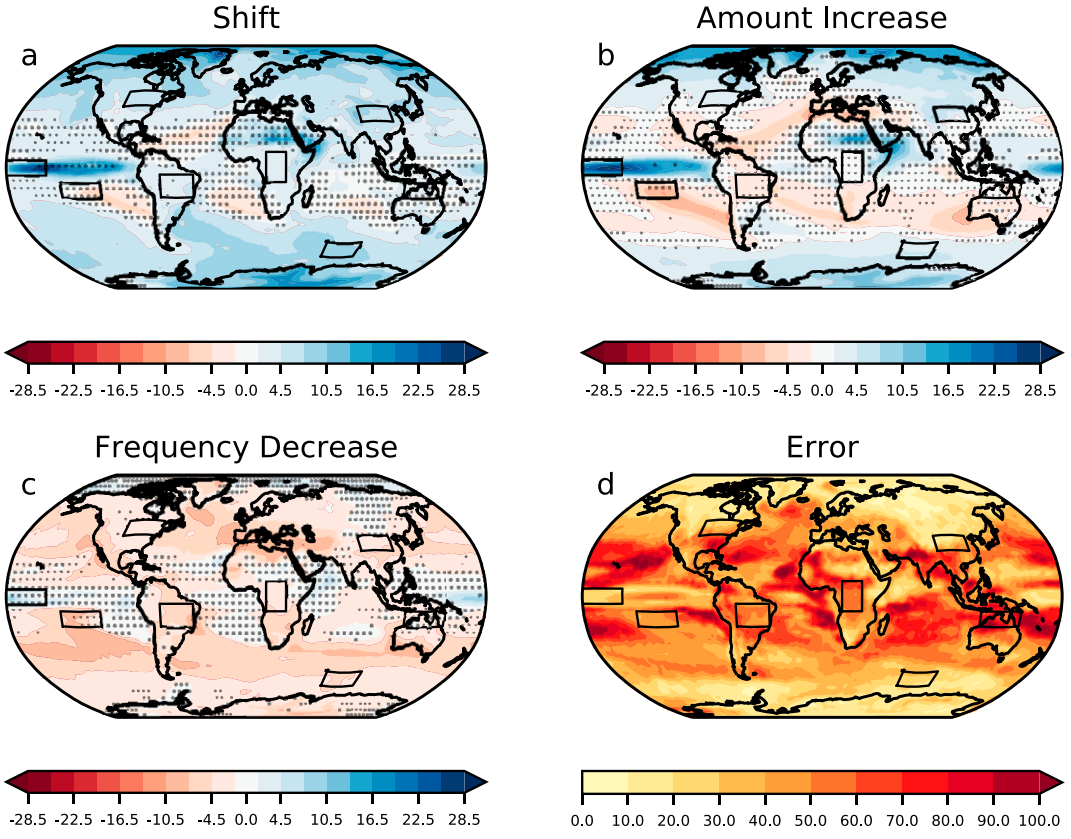

FIG. 4. Idealized mode parameters (% K^{-1}) fitted to the CMIP5 ensemble mean (RCP8.5 − Historical) daily precipitation change intensity distribution at each grid point: (a) shift mode S (the magnitude is the same for both amount and frequency space), (b) amount increase mode I, (c) frequency decrease mode D, and (d) error on the fit in amount space (%). Black boxes show the regions that are used to produce the precipitation distribution changes shown in Figs. 5 and 6. Stippling in (a)–(c) indicates regions where fewer than 80% of CMIP5 models agree on the sign of the mode, when modes are fitted to individual models.

light/moderate rain rates closely, but do not agree with the GCM changes at the ends of the rain-rate spectrum.

There is a small mean decrease in precipitation over the tropical South American region (Figs. 5c,g), and this is reflected in a slightly larger decrease in amount at light/moderate rain rates than the corresponding increase at high rain rates. In this case, the modes capture the magnitude of the light/moderate rain-rate decrease more closely than the high rain-rate increase. Over the tropical African region (Figs. 5d,h) there is a small mean increase in precipitation, and the modes capture the GCM shift from light/moderate to high rain rates.

Over the north Australian region (Figs. 6a,e) the ensemble mean change in precipitation is very small and the error on fitting the modes is large. The modes do capture a decrease in the amount of moderate precipitation but not an increase in very heavy precipitation. In the East Asia region (Figs. 6b,f) there is quite a large increase in mean precipitation, and this is reflected in increases in heavy precipitation being greater than decreases at light/moderate rain rates. This is captured by the modes, but they again overestimate the decreased frequency at low rain rates. The North American region (Figs. 6c,g) is similar to East Asia both in terms of the change in distribution and the agreement of the two-mode model with the GCMs. Finally, the Southern Ocean region (Figs. 6d,h) shifts from low to moderate/high rain rates, and the modes capture this very closely for the higher rain rates but produce larger decreases at low rain rates compared to the GCMs.

c. *Assessment of the two-mode model at various rain rates*

Figure 6 shows the spatial pattern of the change in frequency of precipitation for the CMIP5 ensemble mean, at four different rain rates chosen to sample the main ways in which the precipitation distribution changes (as shown for the globally aggregated change in Fig. 3). To minimize noise, each sample frequency change is calculated as the sum of frequency changes in three adjacent rain-rate bins, with a "very light" rain rate centered in log-space at 0.56 mm day^{-1}, a "light/moderate" rain rate centered at 3.06 mm day^{-1}, a "heavy" rain rate centered at 23.74 mm day^{-1}, and a "very heavy" rain rate centered at 93.05 mm day^{-1}. For comparison, Fig. 6 also shows the estimate of these frequency changes from fitting the two-mode model to the GCM data. At the very heavy rain rate, the two-mode model and GCMs produce

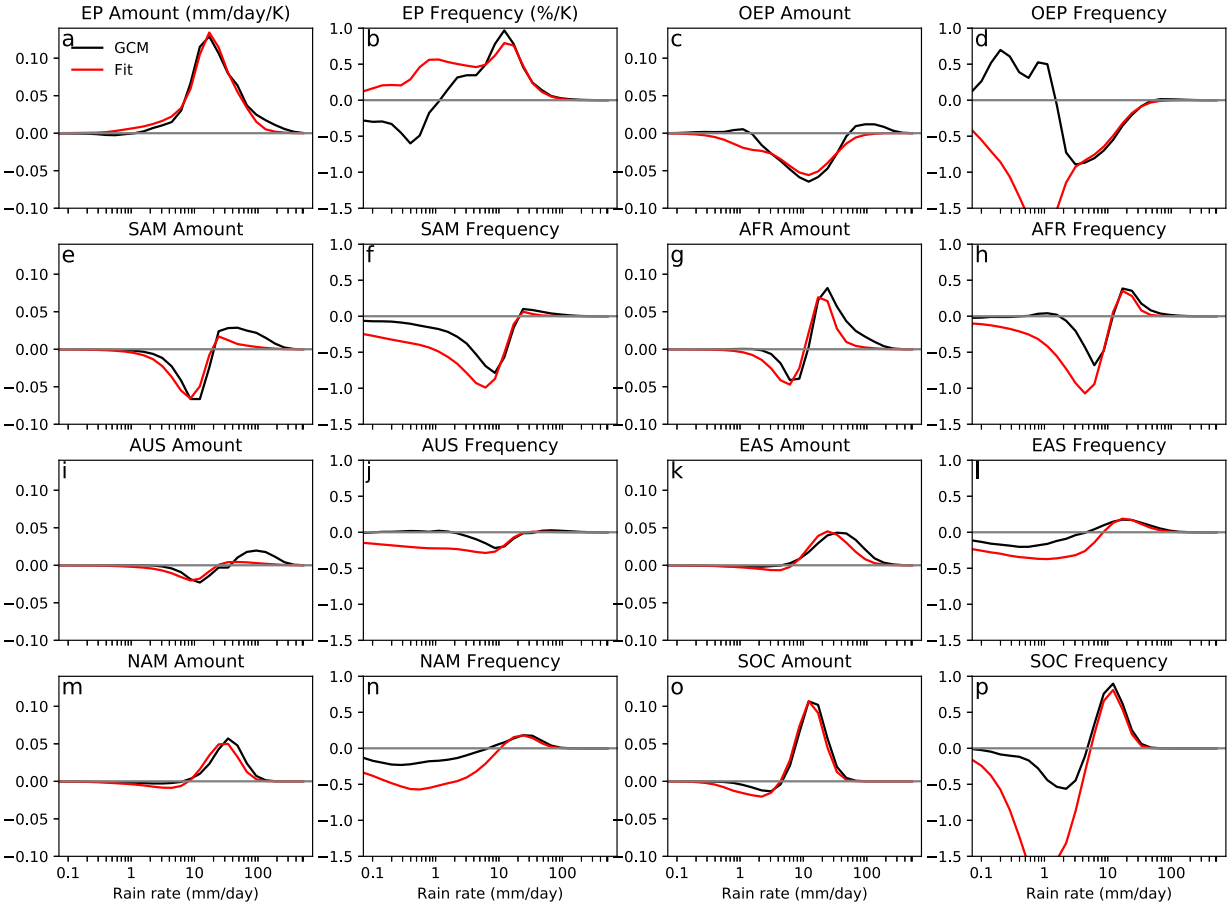

FIG. 5. Regional changes in the precipitation intensity distribution in amount (mm day^{-1} K^{-1}) and frequency space (% K^{-1}) for the CMIP5 ensemble mean (RCP8.5 − Historical). Black lines show the CMIP5 ensemble mean and red lines show the two-mode model fitted to this distribution. Regions are shown as black boxes in Fig. 4. Plots show (a),(b) equatorial Pacific (EP), (c),(d) off-equatorial Pacific (OEP), (e),(f) South America (SAM), (g),(h) African (AFR), (i),(j) Australian (AUS), (k),(l) East Asian (EAS), (m),(n) North American (NAM), and (o),(p) Southern Ocean (SOC) regions.

a similar pattern of frequency change, but the magnitude of increases is larger in GCMs. At the heavy rain rate the two-mode model captures the pattern and magnitude of GCM frequency change across the globe very closely. For the light/moderate rain rate, the two modes also agree closely with the pattern of frequency change in GCMs, but generally show a larger change than the GCMs, particularly in the tropics. At the very light rain rate, the two modes capture the sign but overestimate the magnitude of frequency changes (compared to GCMs) over most land areas and the Arctic, but are generally opposite in sign to the GCM changes over most of the world's oceans. In general, the two-mode model fit appears to show similar features at regional scales as at the global scale, capturing GCM changes in moderate and heavy precipitation but disagreeing with GCM changes at the highest and lowest rain rates.

Overall, the idealized modes agree reasonably well with GCMs on regional scales, with increased frequency/amount at high rain rates and decreased frequency/amount at light/moderate rain rates. Therefore, if the modes can be linked to physical processes then these processes could explain the shift from moderate to high rain rates in GCM projections, and potentially in the real world. In the next section we propose a simple conceptual model that might provide a physical basis for the two modes of precipitation change in regions/seasons where precipitation is dominated by deep convection.

4. A simple conceptual model of the intensity distribution change of deep convective precipitation under warming

In this section, we try to understand the physical basis behind the two idealized modes described in section 3. The frequency decrease and frequency shift modes are used, as they are easier to interpret physically than the equivalent modes in amount space. We limit our scope to deep convective precipitation, which dominates precipitation in GCMs in the tropics, and also plays an important role in summertime midlatitude precipitation.

As described in the introduction, one possible reason for a decreased frequency of moderate precipitation and increased

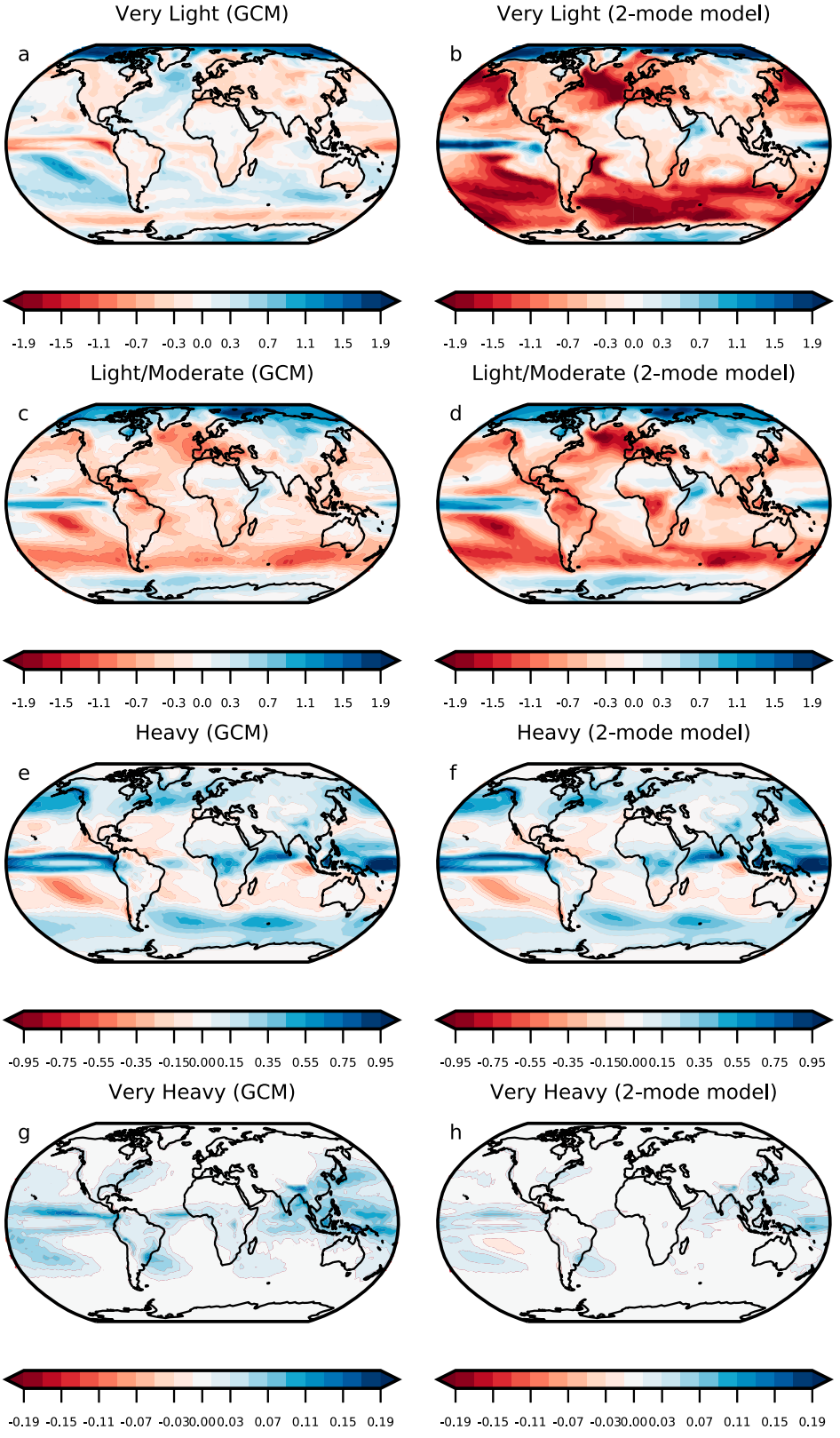

FIG. 6. (left) CMIP5 ensemble mean changes (RCP8.5 − Historical) in the frequency of precipitation (% K^{-1}) in four rain-rate bands. (right) As in the left column, but changes in frequency are estimated by fitting the two-mode model to the CMIP5 ensemble mean changes.

TABLE 2. Summary of notation.

Notation	Meaning
$\overline{x}$	Long-term time-mean value of x
$\langle x \rangle$	Mass-weighted vertical integral of x over the free troposphere
x_i	Value of x for convective event i
x_i'	Value of x for analog future event corresponding to present-day event x_i
x_{diff}	Difference in value of x between end of current and end of previous convective events
Δx	Change in x under warming
$\tilde{x}$	Mean value of x during convective events
$\hat{x}_i$	Mean value of x between end of previous event $(i-1)$ and end of current convective event (i)

frequency and intensity of heavy precipitation in regions dominated by deep convection is because of an increase in CIN under warming, particularly over land. Here, we first try to mathematically formalize this idea and link it to a frequency decrease mode. Given a frequency decrease mode—either driven by CIN changes or by some other mechanism—we then explore the assumptions that are necessary for a frequency shift mode (increased intensity of precipitation events) to also occur. To do this, we build a simple theoretical model of how deep convective rainfall responds to global warming in any particular region, based upon local changes in the dry static energy (DSE) budget.

The derivation of the conceptual model is based upon discrete precipitation "events" and so it might be more appropriate to compare to 3- or 6-hourly precipitation accumulations rather than the daily data that are available from CMIP5. Nevertheless the model does appear to be relevant to changes in daily precipitation intensity. Spatially, the model is based upon GCM-scale grid boxes, where scale separation between convection and the large-scale circulation can be assumed. The notation used in this section is summarized in Table 2.

a. Physical basis of a frequency decrease mode

We first examine a possible physical basis for a frequency decrease mode of convective rainfall under warming, based on changes in CIN. We first assume that for any given grid point, the frequency of rainfall events (f) decreases under warming if local time-mean CIN increases. So, f scales under warming as

$$f \propto g(\overline{\text{CIN}}), \tag{7}$$

where $g(x)$ is some monotonically decreasing function that remains ≥ 0 as $x \to \infty$ (such as $g = 1/x$). The exact functional form of $g(x)$ is not crucial here. Overbars denote a long-term time mean.

We further assume that this scaling applies at each rain rate within the event rainfall distribution for that grid point—that is, only the amplitude of the rainfall distribution varies with $\overline{\text{CIN}}$, not the shape of the distribution.

So we can link our results directly to the two-mode model of Pendergrass and Hartmann (2014b), we will work in log space. Event frequency $f(\ln P)$ scales under warming as

$$f(\ln P) \propto g(\overline{\text{CIN}}), \tag{8}$$

where P is the total (nonzero) rainfall for each event. Now, for a future climate state denoted by a prime,

$$f'(\ln P) \propto g\left(\overline{\text{CIN}'}\right). \tag{9}$$

This gives

$$\frac{\Delta f(\ln P)}{f(\ln P)} = \frac{g\left(\overline{\text{CIN}'}\right)}{g(\overline{\text{CIN}})} - 1. \tag{10}$$

So $f(\ln P)$ scales under warming at a fractional rate that is independent of P. This is equivalent to a frequency decrease mode [cf. Eq. (5)] and in regions where CIN increases this will lead to a decreasing frequency of rainfall events.

In deriving this frequency decrease mode, we have assumed that only the amplitude of the rainfall distribution varies with $\overline{\text{CIN}}$, not the shape of the distribution. However, it seems likely that storms that are strongly dynamically or thermodynamically forced are less likely to be inhibited by this increased CIN (Rasmussen et al. 2017; Kendon et al. 2019). So it is possible that the frequency decrease mode should not apply for the highest daily rain rates. Increased CIN may also not affect precipitation from shallow convection, so the lowest rain rates may be less affected than moderate rain rates. This could partially explain why the two-mode model does not agree with GCM precipitation frequency changes at the lowest and highest rain rates.

We note that as well as or instead of changes in CIN, other possible drivers of change in convective frequency under warming might be related to entrainment or convective organization, which could affect lower tropospheric water vapor, a variable that is closely related to convective initiation (e.g., Kuo et al. 2017).

b. Physical basis of a frequency shift mode

We now examine the assumptions that are necessary for a frequency shift mode to occur (i.e., a shift of the daily precipitation distribution to higher or lower intensities), and how this interacts with a frequency decrease mode. As described above, increased CIN is one possible cause of a frequency decrease mode, but we do not need to assume a CIN-based mechanism in this next piece of analysis, only that a frequency decrease mode occurs for some reason. Rasmussen et al. (2017) proposed that a reduced frequency of convection would lead to an increase in CAPE, due to the greater time available between events for convective instability to build up. Instead of considering CAPE, we examine this question using a simple conceptual model based on the dry static energy budget. A schematic of our model is shown in Fig. 7a.

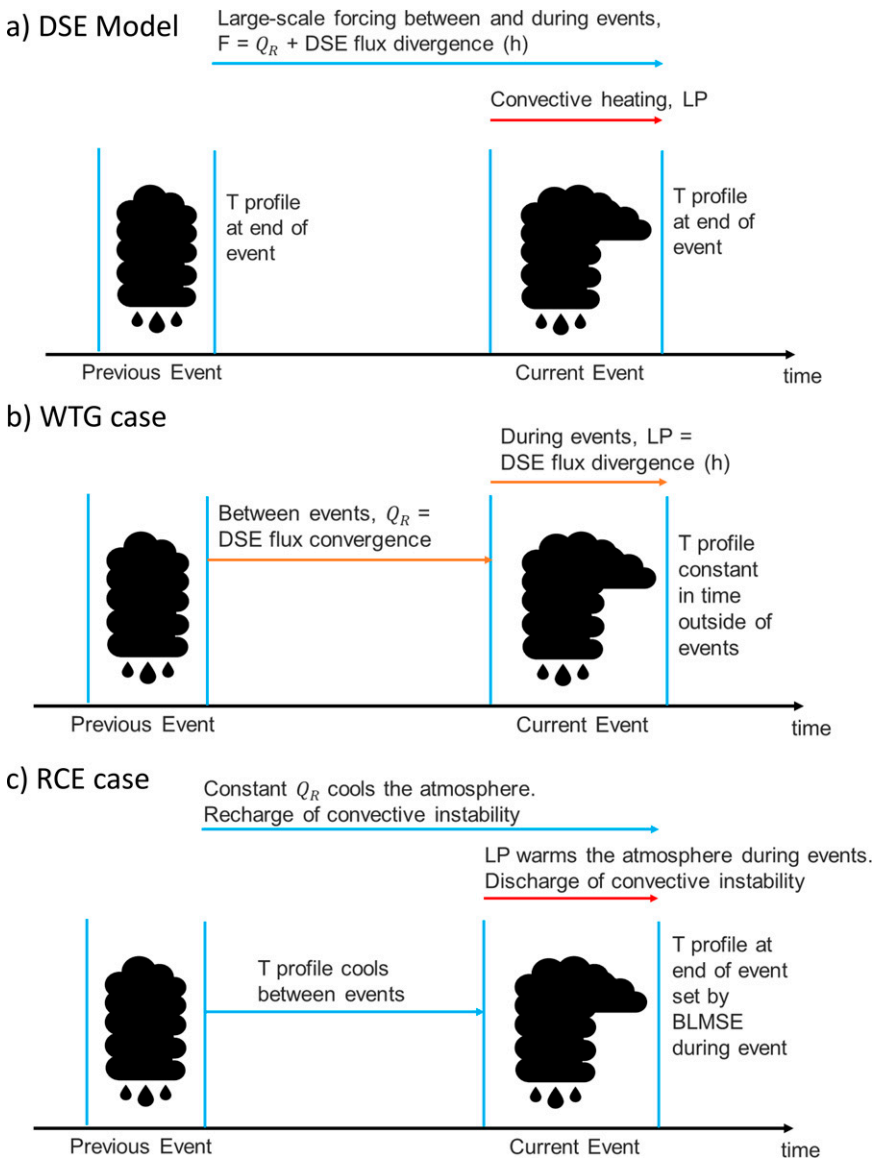

FIG. 7. (a) Schematic of a simple DSE budget model used to connect the two idealized modes to physical processes in regions where precipitation is dominated by deep convection. (b) Schematic of the simple DSE budget model under a version of strict weak temperature gradient (WTG) assumptions. (c) Schematic of the simple DSE budget model under local radiative–convective equilibrium (RCE) assumptions.

We start from the time-varying DSE budget, vertically integrated through the free troposphere (e.g., Muller and O'Gorman 2011) and calculated at each grid point. Dry static energy is defined as $s = c_pT + gZ$, where c_p is the specific heat capacity of air under constant pressure, T is temperature, g is the acceleration due to gravity, and Z is the geopotential height. Following O'Gorman et al. (2012) we omit the boundary layer from our vertical integral so we can neglect surface sensible heat fluxes.

During and between each convective event the free troposphere is cooled or heated at a (nonconstant) rate by radiative cooling and DSE flux divergence/convergence by the large-scale circulation. We define these as the large-scale (GCM grid scale) forcing, F:

$$F = Q_R + h, \tag{11}$$

where Q_R is the radiative cooling rate, h is the DSE flux divergence rate, and all quantities are vertically integrated (with mass weighting) over the free troposphere. In the global mean, F is governed by the net radiative cooling rate of the troposphere, while at the local level DSE flux divergence (i.e., the large-scale circulation) is dominant and so F varies substantially in space (Muller and O'Gorman 2011). The total

large-scale forcing during and between successive convective events is equal to $\int_0^\tau F dt$, where τ is the time between the end of the previous event and the end of the current one (to include forcing during the current event).

We assume that all condensate produced by convection precipitates within the same (GCM scale) grid box during the event. Therefore, the total atmospheric heating provided by each convective event (LP) is balanced by the following DSE budget:

$$LP = \int_0^\tau F dt + \langle c_p(T_{\text{current}} - T_{\text{prev}})\rangle + \langle g(Z_{\text{current}} - Z_{\text{prev}})\rangle, \tag{12}$$

where L is the latent heat of condensation, P is the precipitation during the current convective event, and T and Z denote the temperature and geopotential height profiles at the end of the current or previous convective events. Angle brackets denote mass-weighted vertical integration through the free troposphere.

For convenience, we restate this as

$$LP = \int_0^\tau F dt + \langle c_p T_{\text{diff}}\rangle + \langle g Z_{\text{diff}}\rangle, \tag{13}$$

where $\langle T_{\text{diff}}\rangle \equiv \langle T_{\text{current}} - T_{\text{prev}}\rangle$ and $\langle Z_{\text{diff}}\rangle \equiv \langle Z_{\text{current}} - Z_{\text{prev}}\rangle$.

So, in this model the DSE released by local precipitation is balanced by the cooling of the local atmospheric column between and during events through radiation and advection, combined with changes in energy storage represented by atmospheric temperature and geopotential height differences between convective events.

We now examine how the distribution of event precipitation totals might change under warming as F, τ, $\langle T_{\text{diff}}\rangle$, and $\langle Z_{\text{diff}}\rangle$ change. We do this by first considering the joint population of F, τ, $\langle T_{\text{diff}}\rangle$, and $\langle Z_{\text{diff}}\rangle$ values that correspond to the population of event precipitation totals, P, in the control climate distribution. So each event, with precipitation P_i, will be associated with a particular set of values F_i, τ_i, $\langle T_{\text{diff},i}\rangle$, and $\langle Z_{\text{diff},i}\rangle$.

We then consider the changes that are likely to occur under warming to F_i, τ_i, $\langle T_{\text{diff},i}\rangle$, and $\langle Z_{\text{diff},i}\rangle$ for each event in the population, to produce an analog population of possible future events corresponding to each present-day event. Each analog future set of F_i', τ_i', $\langle T_{\text{diff},i}'\rangle$, and $\langle Z_{\text{diff},i}'\rangle$ produces a new future precipitation P_i' (where primes denote future values). The mapping from P_i to P_i' across all events i determines how the rainfall distribution changes under warming.

So, from Eq. (13), each event i in the precipitation distribution can be expressed as

$$LP_i = \int_0^{\tau_i} F_i dt + \langle c_p T_{\text{diff},i}\rangle + \langle g Z_{\text{diff},i}\rangle. \tag{14}$$

We now need to make some assumptions about how much $\langle T_{\text{diff},i}\rangle$ and $\langle Z_{\text{diff},i}\rangle$ are able to vary in convective environments, and about the balance between DSE flux divergence and local radiative cooling. We choose to examine two opposing idealized cases: 1) a strict version of weak temperature gradient (WTG) assumptions (e.g., Sobel et al. 2001), whereby the local column temperature and geopotential height relax to the local time mean by the end of each convective event, and radiative cooling between events is balanced by weak local subsidence; and 2) local radiative–convective equilibrium, whereby h (the DSE flux divergence rate) is zero and latent heating during each event warms the atmosphere, which then radiatively cools between events. By probing these idealized cases our aim is to discover useful information about the system as a whole. In reality different convective environments will likely combine aspects of both cases, though the idealized WTG case is likely closer to the truth (Jakob et al. 2019), particularly in ascending regimes in the deep tropics.

1) Strict weak temperature gradient case

As stated above, our assumption for this case is that the local column temperature and geopotential height relax to the local time mean by the end of each convective event, and radiative cooling between events is balanced by weak local subsidence. For simplicity we also neglect radiative cooling/heating during convective events, as this is likely to be smaller than other terms. These assumptions are summarized in a schematic in Fig. 7b. Latent heating during each event i is exactly balanced by the total DSE flux divergence integrated over the free troposphere during the event (which we denote as H_i):

$$LP_i = H_i. \tag{15}$$

Under warming, each event i could change its characteristics. Denoting these altered events by primes to produce an analog future population of events gives

$$LP_i' = H_i'. \tag{16}$$

Under WTG assumptions, we can neglect horizontal variations in s to give

$$H_i = \int \left\langle \omega_i \left(\frac{ds}{dp}\right)_i \right\rangle dt, \tag{17}$$

where ω_i is the grid point–scale vertical velocity, $(ds/dp)_i$ is the dry static stability, and the time integral is performed over event i. So it is clear that in order to determine H_i and H_i' we need to know how the large-scale circulation ω_i and dry static stability $(ds/dp)_i$ evolve with time during each convective event and how this changes under warming. In GCMs this is likely to be very sensitive to the particular convective parameterization used. We do not try to predict this directly, but instead discuss possible ways that it might scale under warming.

Perhaps the simplest way that the distribution of H could change under warming is that H_i'/H_i scales in the same way for all events at a given grid point. This scaling excludes those convective events that exist in the present-day distribution but not in the future analog distribution, due to the imposed decrease in convective frequency. As we will see later, making this scaling

assumption is equivalent to assuming a frequency shift mode of the rain-rate distribution. Physically, this assumption could correspond to changes in the mean atmospheric circulation regime at each grid point, which in many cases is related to mean changes in local boundary layer moist static energy (MSE) (Lambert et al. 2017). For example, if local MSE increases relative to the rest of the tropics (as it does in the equatorial Pacific because enhanced SST warming in this region; e.g., Xie et al. 2010) then there will be an increase in local time-mean ascent and there could be an increase in the amount of DSE that each future convective event is able to export out of the column.

Making this simple scaling assumption, and if we define $\tilde{H}$ as the mean value of H_i over all events at a given grid point, then for every event i

$$H_i'/H_i = \tilde{H}'/\tilde{H}. \tag{18}$$

Next, we neglect the DSE flux convergence between events (as we have already assumed that it is exactly balanced by radiative cooling between events) to give [from Eq. (18)]

$$H_i'/H_i = \frac{\hat{h}_i'\,\tau_i'}{\hat{h}_i\,\tau_i}, \tag{19}$$

where h_i is the time-varying DSE flux-convergence rate between the end of the previous event $(i-1)$ and the end of the current event (i), τ_i is the time between the end of the previous event and the end of the current one, and $\hat{h}_i$ denotes the mean of h_i over time period τ_i.

We now assume that the time between events τ_i scales under warming for each event in the same way as the mean time between events $\overline{\tau}$. If $\overline{\tau_i'} > \overline{\tau_i}$ then this assumption imposes a frequency decrease mode (see previous section). From Eq. (19) this gives

$$H_i'/H_i = \frac{\hat{h}_i'\,\overline{\tau'}}{\hat{h}_i\,\overline{\tau}}. \tag{20}$$

Next, taking the mean over events gives

$$\tilde{H}'/\tilde{H} = \frac{\overline{h'}\,\overline{\tau'}}{\overline{h}\,\overline{\tau}}. \tag{21}$$

Now, combining Eqs. (16), (18), and (21) gives

$$\frac{\Delta P_i}{P_i} = \tilde{H}'/\tilde{H} - 1 = \frac{\overline{h'}\,\overline{\tau'}}{\overline{h}\,\overline{\tau}} - 1. \tag{22}$$

As the frequency of events $f = 1/\overline{\tau}$, we then obtain

$$\frac{\Delta P_i}{P_i} = \frac{\overline{h'}}{\overline{h}}\,\frac{f}{f'} - 1. \tag{23}$$

We now have a relationship between the change in the time-mean DSE flux divergence rate $\overline{h}$, the frequency of convective events, and precipitation intensity change. This is constant across all events i, so we can generalize this equation to describe the change in P for all events in the distribution:

$$\frac{\Delta P}{P} = \frac{\overline{h'}}{\overline{h}}\,\frac{f}{f'} - 1. \tag{24}$$

Equation (24) describes a fractionally constant change in precipitation per event at each point in the rainfall distribution at each grid point. It is equivalent to a frequency shift mode of the distribution of event precipitation amounts in log-space (Pendergrass and Hartmann 2014b), given by

$$f'(\ln P) = f\left(\ln P - \frac{\Delta P}{P}\right) = f(\ln P - \text{constant}), \tag{25}$$

where f and f' represent the frequency of events in the control and future event precipitation amount distributions respectively.

So we now have a set of assumptions under which a frequency shift mode arises, and a framework that connects changes in precipitation intensity, frequency, and mean [represented by $\overline{h}$, as can be seen from taking the time mean of (16)]. It can be seen from Eq. (24) that changes in both f and $\overline{h}$ combine to balance the frequency shift mode. A decrease in frequency is balanced by increased intensity of precipitation in each event, while local changes in $\overline{h}$ can increase or decrease the intensity distribution of precipitation events, depending on the sign of $\overline{h}$. In the absence of convective frequency changes, the spatial pattern of the frequency shift mode would exactly follow the pattern of $\overline{h}$, and would therefore (under our strict WTG assumptions) also exactly match the pattern of $\overline{P}$ shown in Fig. 1a. Conversely, in the absence of $\overline{h}$ changes the frequency shift mode would be positive almost everywhere, in order to balance the frequency decrease mode shown in Fig. 4c.

Changes in $\overline{h}$ under warming are associated with changes in both $\overline{\omega}$ and $\overline{ds/dp}$ (Muller and O'Gorman 2011). Due to WTG constraints, $\Delta\left(\overline{ds/dp}\right)$ is relatively constant throughout the tropics, so it tends to reinforce the pattern of climatological $\overline{h}$ (Muller and O'Gorman 2011). Changes in circulation, $\Delta\overline{\omega}$, are much more spatially variable, and include contributions from both the weakening of the overturning circulation and spatial shifts in the regions of convection (Chadwick et al. 2013). Note that due to the diagnostic nature of the DSE budget, this framework makes a connection between changes in the daily distributions of regional precipitation and mean circulation change but does not establish any causality in the relationship.

In summary, strict WTG assumptions suggest that imposed changes in convective frequency and time-mean large-scale DSE divergence would lead to changes in the intensity distribution of precipitation. In the idealized case where H scales in the same way under warming for each event, the distribution change can be exactly represented by a frequency shift mode. In this WTG model, an imposed frequency decrease mode would lead to increased intensity of precipitation in each event, while changes in large-scale circulation can lead to either increases or decreases in intensity depending on the sign of DSE convergence change.

2) LOCAL RADIATIVE–CONVECTIVE EQUILIBRIUM CASE

We now turn to the second (opposing and idealized) case of Eq. (13), representing the rather unrealistic scenario of local radiative–convective equilibrium (RCE). Despite the fact that local RCE does not appear to occur (Jakob et al. 2019), it may still give some insights into how convective precipitation responds to warming when the frequency of events decreases. Our assumption in this case is that DSE flux convergence is zero and latent heating during each event warms the atmosphere, which then radiatively cools between events. These assumptions are summarized in a schematic in Fig. 7c. For each event i, Eq. (13) becomes

$$LP_i = \int_0^{\tau_i} Q_{\mathrm{rad},i}\,dt + \langle c_p T_{\mathrm{diff},i}\rangle + \langle gZ_{\mathrm{diff}}\rangle. \tag{26}$$

We next make the simplifying assumption that Q_{rad} is constant in time at each grid point, neglecting the radiative impacts of time variation of temperature, clouds, and water vapor (which may in fact be important; e.g., Voigt and Shaw 2015). So $Q_{\mathrm{rad},i} = \overline{Q_{\mathrm{rad}}}$ at each grid point, giving

$$LP_i = \overline{Q_{\mathrm{rad}}}\,\tau_i + \langle c_p T_{\mathrm{diff},i}\rangle + \langle gZ_{\mathrm{diff}}\rangle. \tag{27}$$

So under warming, the change in precipitation for each event i is given by

$$\frac{\Delta P_i}{P_i} = \frac{\Delta\overline{Q_{\mathrm{rad}}}\,\tau_i + \Delta\langle c_p T_{\mathrm{diff},i}\rangle + \Delta\langle gZ_{\mathrm{diff}}\rangle}{\overline{Q_{\mathrm{rad}}}\,\tau_i + \langle c_p T_{\mathrm{diff},i}\rangle + \langle gZ_{\mathrm{diff}}\rangle}. \tag{28}$$

We now assume that $\langle T\rangle$ at the end of each convective event is a moist adiabat corresponding to boundary layer MSE (BLMSE) during the event. Therefore, $\langle T_{\mathrm{diff},i}\rangle$ is a function of the difference in BLMSE between successive convective events.

We next make the simplifying assumption that the value of BLMSE during convective events does not vary much between successive events (note that this assumption is likely to fail for the strongest and weakest convective events). In this case, $\langle c_p T_{\mathrm{diff},i}\rangle \approx 0$ and $\langle gZ_{\mathrm{diff},i}\rangle \approx 0$ for both the present-day and future-analog cases, and we obtain

$$\frac{\Delta P_i}{P_i} = \frac{\overline{Q'_{\mathrm{rad}}}\,\tau'_i}{\overline{Q_{\mathrm{rad}}}\,\tau_i} - 1. \tag{29}$$

As we did in the WTG case, we again impose a frequency decrease mode by assuming that the time between events τ_i scales under warming for each event in the same way as the mean time between events $\overline{\tau}$. Replacing $\overline{\tau}$ with $1/f$ gives

$$\frac{\Delta P}{P} = \frac{\overline{Q'_{\mathrm{rad}}}}{\overline{Q_{\mathrm{rad}}}}\,\frac{f}{f'} - 1, \tag{30}$$

which is constant for all events and once again is equivalent to a frequency shift mode in log-space [see Eq. (25)].

As in the WTG case, a decrease in convective frequency implies an increase in precipitation intensity, and here the other factor is the change in $\overline{Q_{\mathrm{rad}}}$. In this local RCE case, Eq. (30) represents a recharge–discharge model of convection, where convective instability is built up between events by radiative cooling, then discharged by latent heating. Under warming, the total amount of recharge is affected by both changes in $\overline{Q_{\mathrm{rad}}}$ and changes in frequency, and these are balanced by changes in the discharge intensity LP. In this case the frequency shift mode arises naturally from the imposition of a frequency decrease mode, as opposed to the strict WTG case where we also need to make an assumption about how H scales in each event in order to obtain a frequency shift mode.

In summary, local RCE assumptions imply a recharge–discharge model of convective instability, with Q_{rad} between events being balanced by LP during events. Under warming, an imposed frequency decrease mode increases the recharge time between events and, combined with changes in Q_{rad}, changes the intensity of precipitation during events. Under certain assumptions, this leads to a frequency shift mode in the intensity distribution of precipitation. The most intense convective events, with anomalously high boundary layer MSE, are not well represented by the assumption that BLMSE does not change much between successive events, and so precipitation extremes may scale differently from other events.

5. Summary and conclusions

We have examined how regional daily precipitation intensity distributions change under warming in future GCM projections. A two-mode model is able to capture CMIP5 ensemble mean regional changes in light/moderate and heavy precipitation reasonably closely. Therefore, the two parameters of this model provide a useful way of quantifying changes in the daily precipitation distribution at regional scales. In general there is an increased frequency of heavy precipitation and a decreased frequency of light/moderate precipitation, but with substantial regional variations. However, in some regions, generally where the mean precipitation change is small, the error of the two-mode fit is high. GCM changes in very heavy and very light precipitation are not captured by the two-mode model. One interpretation of this is that the top and bottom ends of the distribution respond differently to warming than the bulk of the precipitation distribution.

Strong spatial variability in the magnitude of the shift mode indicates that the Clausius–Clapeyron relationship does not primarily control the overall magnitude of the shift to heavier rain rates, as increases in low-level moisture under warming display relatively little spatial variability (Chadwick et al. 2016). This analysis cannot assess the relative influence of moisture increases on precipitation extremes, which are not well described by the two-mode model, but previous work has found a strong dynamical influence on regional changes in precipitation extremes (Pfahl et al. 2017), as well as a strong connection between regional changes in mean and extreme precipitation (Nishant and Sherwood 2021).

For deep convective precipitation, a simple conceptual model based on the DSE budget was developed in order to provide a possible physical basis for the two-mode model. Regional precipitation is strongly related to the large-scale circulation and is constrained by energetic considerations. In

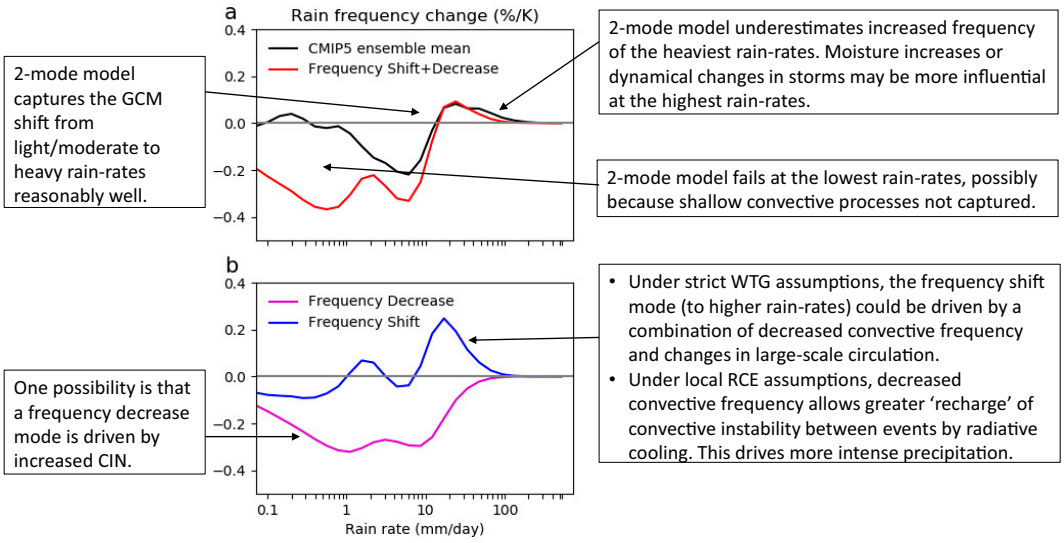

FIG. 8. Summary of the two-mode model and link to the DSE budget model, showing CMIP5 ensemble mean changes (RCP8.5 − Historical) in the tropically aggregated daily precipitation intensity distribution in frequency space. (a) Black line shows GCM changes and red line shows the combination of frequency shift and frequency decrease modes fitted to the GCM changes. (b) Blue and purple lines show the individual contributions of frequency shift and frequency decrease modes to the fit, respectively.

order for precipitation in any region to increase, it generally must export more DSE, usually through a change in large-scale circulation (e.g., Muller and O'Gorman 2011). So some other regions must adjust by importing more DSE. Therefore, changes in regional precipitation and large-scale circulation are not free to respond only to local changes (e.g., in moisture); rather, they are also constrained by how much extra DSE other regions can take up. This applies most obviously for time-mean precipitation but is also likely to constrain changes in the distribution of daily precipitation.

Our analysis shows how an increase in CIN could potentially lead to a frequency decrease mode, although we note that this is not the only reason that convective frequency might decrease under warming. In the tropics, a form of strict weak temperature gradient assumptions provides a framework in which changes in precipitation intensity are balanced by changes in mean DSE convergence (i.e., large-scale circulation), combined with changes in convective frequency. An alternative, local radiative–convective equilibrium (RCE) framework emphasizes the role of local radiative cooling, also combined with changes in frequency. Although local RCE is not realistic, certain aspects of this model may be relevant outside of the deep tropics, where WTG assumptions are less applicable. A number of strict simplifying assumptions are necessary in order for this DSE model to produce exact frequency decrease and frequency shift modes, so it is unsurprising that GCM projections deviate to some extent from the two-mode model. For changes at the lowest rain rates, transitions between deep and shallow convection, which are not included in our DSE model, may be influential. A summary of our interpretation of the two-mode model and its link to the conceptual DSE model is shown in Fig. 8.

Acknowledgments. Robin Chadwick was supported by the Newton Fund through the Met Office Climate Science for Service Partnership Brazil (CSSP Brazil). Portions of this study were supported by the Regional and Global Model Analysis (RGMA) component of the Earth and Environmental System Modeling Program of the U.S. Department of Energy's Office of Biological and Environmental Research (BER) via National Science Foundation IA 1947282. We thank Ségolène Berthou, Wenxia Zhang, Gill Martin, Adrian Lock, Ian Boutle, and Mike Whitall for useful discussions, and three anonymous reviewers for comments that significantly improved the quality of the manuscript.

Data availability statement. The CMIP5 data used in this study are freely available to download from the Earth System Grid.

APPENDIX

Derivation of Conversion between Amount Space and Frequency Space Modes

From Eq. (10) in Pendergrass and Hartmann (2014b), we obtain the following two equations:

$$I_A \sum A^2 - S_A \sum A \frac{dA}{d\ln P} = \sum A \Delta A, \tag{A1}$$

$$- I_A \sum A \frac{dA}{d\ln P} + S_A \sum \frac{dA}{d\ln P}^2 = -\sum \frac{dA}{d\ln P} \Delta A, \tag{A2}$$

where I_A is the increase mode parameter and S_A is the shift parameter, both in amount space; A is the amount of precipitation in each rain-rate bin, P is the rain rate, and sums are taken over all rain-rate bins; and ΔA denotes the change in the amount of precipitation in each rain-rate bin under warming, in the GCM to which the parameters are being fitted.

Constructing the equivalent set of equations in frequency space gives

$$I_f \sum A^2 + S_f \sum \left(A^2 - A \frac{dA}{d\ln P} \right) = \sum A \Delta A, \tag{A3}$$

$$I_f \sum A \left(A - \frac{dA}{d\ln P} \right) + S_f \sum \left(A - \frac{dA}{d\ln P}^2 \right) = -\sum \left(A - \frac{dA}{d\ln P} \right) \Delta A, \tag{A4}$$

where I_f is the increase mode parameter and S_f is the shift parameter, in this case in frequency space.

Equation (A3) can be rearranged to give

$$(S_f + I_f) \sum A^2 - S_f \sum A \frac{dA}{d\ln P} = \sum A \Delta A, \tag{A5}$$

and Eqs. (A4) and (A5) can be combined to obtain

$$-(S_f + I_f) \sum A \frac{dA}{d\ln P} + S_f \sum \frac{dA}{d\ln P}^2 = -\sum \frac{dA}{d\ln P} \Delta A. \tag{A6}$$

Comparing Eq. (A1) with Eq. (A5) and Eq. (A2) with Eq. (A6) it can be seen that one solution of this system of equations, linking the amount space and frequency space parameters, is

$$I_A = S_f + I_f \text{ and} \tag{A7}$$

$$S_A = S_f. \tag{A8}$$

As the shift parameters in amount space and frequency space are equal [see Eq. (A8)], we now define a single shift parameter, $S \equiv S_A = S_f$. As the increase mode in frequency space is in fact generally negative, we denote this as a decrease mode, $D \equiv I_f$, and refer to the increase mode in amount space simply as $I \equiv I_A$.

REFERENCES

Abbott, T., and T. Cronin, 2021: Aerosol invigoration of atmospheric convection through increases in humidity. *Science*, **371**, 6524–85, https://doi.org/10.1126/science.abc5181.

Alexander, L., and Coauthors, 2006: Global observed changes in daily climate extremes of temperature and precipitation. *J. Geophys. Res.*, **111**, D05109, https://doi.org/10.1029/2005JD006290.

Allan, R. P., B. J. Soden, V. O. John, W. Ingram, and P. Good, 2010: Current changes in tropical precipitation. *Environ. Res. Lett.*, **5**, 025205, https://doi.org/10.1088/1748-9326/5/2/025205.

——, C. Liu, M. Zahn, D. Lavers, E. Koukouvagias, and A. Bodas-Salcedo, 2014: Physically consistent responses of the global atmospheric hydrological cycle in models and observations. *Surv. Geophys.*, **35**, 533–552, https://doi.org/10.1007/s10712-012-9213-z.

Allen, M. R., and W. J. Ingram, 2002: Constraints on future changes in climate and the hydrologic cycle. *Nature*, **419**, 228–232, https://doi.org/10.1038/nature01092.

Bador, M., M. Donat, O. Geoffroy, and L. Alexander, 2018: Assessing the robustness of future extreme precipitation intensification in the CMIP5 ensemble. *J. Climate*, **31**, 6505–6525, https://doi.org/10.1175/JCLI-D-17-0683.1.

Bentsen, M., and Coauthors, 2013: The Norwegian Earth System Model, NorESM1-M—Part 1: Description and basic evaluation of the physical climate. *Geosci. Model Dev.*, **6**, 687–720, https://doi.org/10.5194/gmd-6-687-2013.

Berg, A., and Coauthors, 2016: Land–atmosphere feedbacks amplify aridity increase over land under global warming. *Nat. Climate Change*, **6**, 869–874, https://doi.org/10.1038/nclimate3029.

Bi, D., and Coauthors, 2013: The ACCESS coupled model: Description, control climate and evaluation. *Aust. Meteor. Oceanogr. J.*, **63**, 41–64, https://doi.org/10.22499/2.6301.004.

Brown, J. R., A. F. Moise, and R. A. Colman, 2017: Projected increases in daily to decadal variability of Asian-Australian monsoon rainfall. *Geophys. Res. Lett.*, **44**, 5683–5690, https://doi.org/10.1002/2017GL073217.

Byrne, M. P., and P. A. O'Gorman, 2016: Understanding decreases in land relative humidity with global warming: Conceptual model and GCM simulations. *J. Climate*, **29**, 9045–9061, https://doi.org/10.1175/JCLI-D-16-0351.1.

Chadwick, R., I. Boutle, and G. Martin, 2013: Spatial patterns of precipitation change in CMIP5: Why the rich do not get richer in the tropics. *J. Climate*, **26**, 3803–3822, https://doi.org/10.1175/JCLI-D-12-00543.1.

——, P. Good, and K. Willett, 2016: A simple moisture advection model of specific humidity change over land in response to SST warming. *J. Climate*, **29**, 7613–7632, https://doi.org/10.1175/JCLI-D-16-0241.1.

Chen, J., A. Dai, Y. Zhang, and K. Rasmussen, 2020: Changes in convective available potential energy and convective inhibition under global warming. *J. Climate*, **33**, 2025–2050, https://doi.org/10.1175/JCLI-D-19-0461.1.

Christenson, J., and Coauthors, 2013: Climate phenomena and their relevance for future regional climate change. *Climate Change 2013: The Physical Science Basis*, T. F. Stocker et al., Eds., Cambridge University Press, 1217–1308.

Chylek, P., J. Li, M. Dubey, M. Wang, and G. Lesins, 2011: Observed and model simulated 20th century Arctic temperature variability: Canadian Earth System Model CanESM2. *Atmos. Chem. Phys. Discuss.*, **11**, 893–907, https://doi.org/10.5194/acpd-11-22893-2011.

Collins, M., and Coauthors, 2013: Long-term climate change: Projections, commitments and irreversibility. *Climate Change 2013: The Physical Science Basis*, T. F. Stocker et al., Eds., Cambridge University Press, 1029–1136.

Dai, A., R. Rasmussen, C. Liu, K. Ikeda, and A. Prein, 2017: A new mechanism for warm-season precipitation response to global warming based on convection-permitting simulations. *Climate Dyn.*, **55**, 343–368, https://doi.org/10.1007/s00382-017-3787-6.

Donat, M., and Coauthors, 2013: Updated analyses of temperature and precipitation extreme indices since the beginning of the twentieth century: The HadEX2 dataset. *J. Geophys. Res. Atmos.*, **118**, 2098–2118, https://doi.org/10.1002/jgrd.50150.

Donner, L., and Coauthors, 2011: The dynamical core, physical parameterizations, and basic simulation characteristics of the atmospheric component AM3 of the GFDL global coupled

model CM3. *J. Climate*, **24**, 3484–3519, https://doi.org/10.1175/2011JCLI3955.1.

Douville, H., and A. John, 2021: Fast adjustment versus slow SST-mediated response of daily precipitation statistics to abrupt 4xCO2. *Climate Dyn.*, **56**, 1083–1104, https://doi.org/10.1007/s00382-020-05522-w.

——, and Coauthors, 2021: Water cycle changes. *Climatic Change 2021: The Physical Science Basis*. Cambridge University Press, https://www.ipcc.ch/report/sixth-assessment-report-working-group-i/, in press.

Dufresne, J. L., and Coauthors, 2013: Climate change projections using the IPSL-CM5 Earth System Model: From CMIP3 to CMIP5. *Climate Dyn.*, **40**, 2123–2165, https://doi.org/10.1007/s00382-012-1636-1.

Dunne, J. P., and Coauthors, 2012: GFDL-ESM2 global coupled climate–carbon Earth system models. Part I: Physical formulation and baseline simulation characteristics. *J. Climate*, **25**, 6646–6665, https://doi.org/10.1175/JCLI-D-11-00560.1.

Emori, S., and S. J. Brown, 2005: Dynamic and thermodynamic changes in mean and extreme precipitation under changed climate. *Geophys. Res. Lett.*, **32**, L17706, https://doi.org/10.1029/2005GL023272.

Fischer, E. M., and R. Knutti, 2016: Observed heavy precipitation increase confirms theory and early models. *Nat. Climate Change*, **6**, 986–991, https://doi.org/10.1038/nclimate3110.

——, J. Sedláček, E. Hawkins, and R. Knutti, 2014: Models agree on forced response pattern of precipitation and temperature extremes. *Geophys. Res. Lett.*, **41**, 8554–8562, https://doi.org/10.1002/2014GL062018.

Fowler, H., and Coauthors, 2021: Anthropogenic intensification of short-duration rainfall extremes. *Nat. Rev. Earth Environ.*, **2**, 107–122, https://doi.org/10.1038/s43017-020-00128-6.

Grabowski, W., and A. Prein, 2019: Separating dynamic and thermodynamic impacts of climate change on daytime convective development over land. *J. Climate*, **32**, 5213–5234, https://doi.org/10.1175/JCLI-D-19-0007.1.

Hazeleger, W., and Coauthors, 2010: EC-Earth: A seamless Earth-system prediction approach in action. *Bull. Amer. Meteor. Soc.*, **91**, 1357–1364, https://doi.org/10.1175/2010BAMS2877.1.

He, J., and B. J. Soden, 2015: Anthropogenic weakening of the tropical circulation: The relative roles of direct CO_2 forcing and sea surface temperature change. *J. Climate*, **28**, 8728–8742, https://doi.org/10.1175/JCLI-D-15-0205.1.

Held, I. M., and B. J. Soden, 2006: Robust responses of the hydrological cycle to global warming. *J. Climate*, **19**, 5686–5699, https://doi.org/10.1175/JCLI3990.1.

Hourdin, F., and Coauthors, 2006: The LMDZ4 general circulation model: Climate performance and sensitivity to parametrized physics with emphasis on tropical convection. *Climate Dyn.*, **27**, 787–813, https://doi.org/10.1007/s00382-006-0158-0.

Jakob, C., M. Singh, and L. Jungandreas, 2019: Radiative convective equilibrium and organized convection: An observational perspective. *J. Geophys. Res. Atmos.*, **124**, 5418–5430, https://doi.org/10.1029/2018JD030092.

Jeffrey, M., L. Rotstayn, M. Collier, S. Dravitzki, C. Hamalainen, C. Moeseneder, K. Wong, and J. Syktus, 2013: Australian CMIP5 submission using the CSIRO-Mk3.6 model. *Aust. Meteor. Oceanogr. J.*, **63**, 1–13, https://doi.org/10.22499/2.6301.001.

Ji, D., and Coauthors, 2014: Description and basic evaluation of Beijing Normal University Earth System Model (BNU-ESM) version 1. *Geosci. Model Dev.*, **7**, 2039–2064, https://doi.org/10.5194/gmd-7-2039-2014.

Kendon, E., R. Stratton, S. Tucker, J. Marsham, S. Berthou, D. Rowell, and C. Senior, 2019: Enhanced future changes in wet and dry extremes over Africa at convection-permitting scale. *Nat. Commun.*, **10**, 1794, https://doi.org/10.1038/s41467-019-09776-9.

Kuo, Y.-H., J. D. Neelin, and C. R. Mechoso, 2017: Tropical convective transition statistics and causality in the water vapor precipitation relation. *J. Atmos. Sci.*, **74**, 915–931, https://doi.org/10.1175/JAS-D-16-0182.1.

Lambert, F. H., A. J. Ferraro, and R. Chadwick, 2017: Land–ocean shifts in tropical precipitation linked to surface temperature and humidity change. *J. Climate*, **30**, 4527–4545, https://doi.org/10.1175/JCLI-D-16-0649.1.

Li, L., and Coauthors, 2013: The Flexible Global Ocean–Atmosphere–Land System Model, Grid-point version 2: FGOALS-g2. *Adv. Atmos. Sci.*, **30**, 543–560, https://doi.org/10.1007/s00376-012-2140-6.

Martin, G. M., and Coauthors, 2011: The HadGEM2 family of Met Office Unified Model climate configurations. *Geosci. Model Dev.*, **4**, 723–757, https://doi.org/10.5194/gmd-4-723-2011.

Mehran, A., A. AghaKouchak, and T. Phillips, 2014: Evaluation of CMIP5 continental precipitation simulations relative to satellite-based gauge-adjusted observations. *J. Geophys. Res. Atmos.*, **119**, 1695–1707, https://doi.org/10.1002/2013JD021152.

Min, S. K., X. Zhang, F. W. Zwiers, and G. C. Hegerl, 2011: Human contribution to more-intense precipitation extremes. *Nature*, **470**, 378–381, https://doi.org/10.1038/nature09763.

Muller, C., and P. O'Gorman, 2011: An energetic perspective on the regional response of precipitation to climate change. *Nat. Climate Change*, **1**, 266–271, https://doi.org/10.1038/nclimate1169.

Neale, R., and Coauthors, 2010: Description of the NCAR Community Atmosphere Model (CAM 4.0). NCAR Tech. Rep NCAR/TN-485+STR, 224 pp.

Nishant, N., and S. Sherwood, 2021: How strongly are mean and extreme precipitation coupled? *Geophys. Res. Lett.*, **48**, https://doi.org/10.1029/2020GL092075.

O'Gorman, P., 2015: Precipitation extremes under climate change. *Curr. Climate Change Rep.*, **1**, 49–59, https://doi.org/10.1007/s40641-015-0009-3.

——, R. Allan, M. Byrne, and M. Previdi, 2012: Energetic constraints on precipitation under climate change. *Surv. Geophys.*, **33**, 585–608, https://doi.org/10.1007/s10712-011-9159-6.

Oueslati, B., P. Yiou, and A. Jezequel, 2019: Revisiting the dynamic and thermodynamic processes driving the record-breaking January 2014 precipitation in the southern UK. *Sci. Rep.*, **9**, 2859, https://doi.org/10.1038/s41598-019-39306-y.

Pall, P., M. R. Allen, and D. A. Stone, 2007: Testing the Clausius-Clapeyron constraint on changes in extreme precipitation under CO_2 warming. *Climate Dyn.*, **28**, 351–363, https://doi.org/10.1007/s00382-006-0180-2.

Pascale, S., W. Boos, S. Bordoni, T. Delworth, S. Kapnick, H. Murakami, G. Vecchi, and W. Zhang, 2017: Weakening of the North American monsoon with global warming. *Nat. Climate Change*, **7**, 806–812, https://doi.org/10.1038/nclimate3412.

Pendergrass, A., and D. Hartmann, 2014a: Changes in the distribution of rain frequency and intensity in response to global warming. *J. Climate*, **27**, 8372–8383, https://doi.org/10.1175/JCLI-D-14-00183.1.

——, and ——, 2014b: Two modes of change of the distribution of rain. *J. Climate*, **27**, 8357–8371, https://doi.org/10.1175/JCLI-D-14-00182.1.

——, R. Knutti, F. Lehner, C. Deser, and B. Sanderson, 2017: Precipitation variability increases in a warmer climate. *Sci. Rep.*, **7**, 17966, https://doi.org/10.1038/s41598-017-17966-y.

Pfahl, S., P. O'Gorman, and E. M. Fischer, 2017: Understanding the regional pattern of projected future changes in extreme precipitation. *Nat. Climate Change*, **7**, 423–427, https://doi.org/10.1038/nclimate3287.

Polade, S. D., D. W. Pierce, D. R. Cayan, A. Gershunov, and M. D. Dettinger, 2014: The key role of dry days in changing regional climate and precipitation regimes. *Sci. Rep.*, **4**, 4364, https://doi.org/10.1038/srep04364.

Rasmussen, K., A. Prein, R. Rasmussen, K. Ikeda, and C. Liu, 2017: Changes in the convective population and thermodynamic environments in convection-permitting regional climate simulations over the United States. *Climate Dyn.*, **55**, 383–408, https://doi.org/10.1007/s00382-017-4000-7.

Scoccimarro, E., and Coauthors, 2011: Effects of tropical cyclones on ocean heat transport in a high-resolution coupled general circulation model. *J. Climate*, **24**, 4368–4384, https://doi.org/10.1175/2011JCLI4104.1.

Seager, R., N. Naik, and G. A. Vecchi, 2010: Thermodynamic and dynamic mechanisms for large-scale changes in the hydrological cycle in response to global warming. *J. Climate*, **23**, 4651–4668, https://doi.org/10.1175/2010JCLI3655.1.

Shepherd, T. G., 2014: Atmospheric circulation as a source of uncertainty in climate change projections. *Nat. Geosci.*, **7**, 703–708, https://doi.org/10.1038/ngeo2253.

Sobel, A. H., J. Nilsson, and L. M. Polvani, 2001: The weak temperature gradient approximation and balanced tropical moisture waves. *J. Atmos. Sci.*, **58**, 3650–3665, https://doi.org/10.1175/1520-0469(2001)058<3650:TWTGAA>2.0.CO;2.

Stephens, G. L., and T. D. Ellis, 2008: Controls of global-mean precipitation increases in global warming GCM experiments. *J. Climate*, **21**, 6141–6155, https://doi.org/10.1175/2008JCLI2144.1.

Stevens, B., and Coauthors, 2013: Atmospheric component of the MPI-M Earth system model: ECHAM6. *J. Adv. Model. Earth Syst.*, **5**, 146–172, https://doi.org/10.1002/jame.20015.

Sun, Y., S. Solomon, A. Dai, and R. W. Portmann, 2007: How often will it rain? *J. Climate*, **20**, 4801–4818, https://doi.org/10.1175/JCLI4263.1.

Taylor, K. E., R. J. Stouffer, and G. A. Meehl, 2012: A summary of the CMIP5 experiment design. *Bull. Amer. Meteor. Soc.*, **93**, 485–498, https://doi.org/10.1175/BAMS-D-11-00094.1.

Trenberth, K., 1999: Conceptual framework for changes of extremes of the hydrological cycle with climate change. *Climatic Change*, **42**, 327–339, https://doi.org/10.1023/A:1005488920935.

Voigt, A., and T. A. Shaw, 2015: Circulation response to warming shaped by radiative changes of clouds and water vapour. *Nat. Geosci.*, **8**, 102–106, https://doi.org/10.1038/ngeo2345.

Voldoire, A., and Coauthors, 2013: The CNRM-CM5.1 global climate model: Description and basic evaluation. *Climate Dyn.*, **40**, 2091–2121, https://doi.org/10.1007/s00382-011-1259-y.

Volodin, E., N. Dianskii, and A. Gusev, 2010: Simulating present-day climate with the INMCM4.0 coupled model of the atmospheric and oceanic general circulations. *Izv., Atmos. Ocean. Phys.*, **46**, 414–431, https://doi.org/10.1134/S000143381004002X.

Wang, B., and Coauthors, 2020: Monsoons climate change assessment. *Bull. Amer. Meteor. Soc.*, **102** (1), E1–E19, https://doi.org/10.1175/BAMS-D-19-0335.1.

Watanabe, M., and Coauthors, 2010: Improved climate simulation by MIROC5: Mean states, variability, and climate sensitivity. *J. Climate*, **23**, 6312–6335, https://doi.org/10.1175/2010JCLI3679.1.

Watanabe, S., and Coauthors, 2011: MIROC-ESM 2010: Model description and basic results of CMIP5-20c3m experiments. *Geosci. Model Dev.*, **4**, 845–872, https://doi.org/10.5194/gmd-4-845-2011.

Xie, S.-P., C. Deser, G. A. Vecchi, J. Ma, H. Teng, and A. T. Wittenberg, 2010: Global warming pattern formation: Sea surface temperature and rainfall. *J. Climate*, **23**, 966–986, https://doi.org/10.1175/2009JCLI3329.1.

Yukimoto, S., and Coauthors, 2012: A new global climate model of the Meteorological Research Institute: MRI-CGCM3—Model description and basic performance. *J. Meteor. Soc. Japan*, **90A**, 23–64, https://doi.org/10.2151/jmsj.2012-A02.

Zhang, W., and T. Zhou, 2019: Significant increases in extreme precipitation and the associations with global warming over the global land monsoon regions. *J. Climate*, **32**, 8465–8488, https://doi.org/10.1175/JCLI-D-18-0662.1.